

Geophysical Research Letters®

RESEARCH LETTER

10.1029/2023GL107308

Characteristics of Station-Derived Convective Cold Pools Over Equatorial Africa



Key Points:

- 4,218 cold pools are identified across equatorial Africa based on temperature and wind criteria
- The occurrence and intensity of the observed cold pools are related to low-level moisture conditions and the depth of convection
- The identified cold pool gust fronts closely correlate with satellite-observed brightness temperature discontinuities

Supporting Information:

Supporting Information may be found in the online version of this article.




Correspondence to:

J. Hoeller,
jannik.hoeller@leibniz-zmt.de

Citation:

Hoeller, J., Haerter, J. O., & Da Silva, N. A. (2024). Characteristics of station-derived convective cold pools over equatorial Africa. *Geophysical Research Letters*, 51, e2023GL107308. <https://doi.org/10.1029/2023GL107308>

Received 14 NOV 2023
Accepted 1 MAR 2024

Jannik Hoeller^{1,2} , Jan O. Haerter^{1,2,3,4} , and Nicolas A. Da Silva¹ 

¹Integrated Modeling, Leibniz Centre for Tropical Marine Research, Bremen, Germany, ²Niels Bohr Institute, Copenhagen University, Copenhagen, Denmark, ³Physics and Earth Sciences, Constructor University Bremen, Bremen, Germany, ⁴Department of Physics and Astronomy, University of Potsdam, Potsdam, Germany

Abstract Due to their potential role in organizing tropical mesoscale convective systems, a better understanding of cold pool (CP) dynamics in such regions is critical, particularly over land where the diurnal cycle further concentrates convective activity. Numerical models help disentangle the processes involved but often lack observational benchmarks. To close this gap, we analyze nearly 43 years of five-minute resolution near-surface timeseries, recorded from 12 automatic weather stations across equatorial Africa during 2019–2023. We identify 4,218 CPs based on criteria for temperature and wind. The identified CP gust fronts, which exhibit respective median temperature and specific humidity decreases of 5.3 K and 2.8 g kg⁻¹, closely correlate with satellite-observed brightness temperature discontinuities. Despite weak diurnal variation in precipitation, observed CP occurrence shows a pronounced diurnal cycle with an afternoon peak — a feature we attribute to low-level moisture conditions. Our findings can serve as observational benchmark to improve simulations of CP organization.

Plain Language Summary Convective cold pools form when rain evaporates underneath thunderstorm clouds. The evaporation causes the air to cool and sink toward the ground, where it is deflected horizontally. Cold pools are thus associated with strong gusty winds, and over tropical land, they can be especially vigorous. Cold pools are also suggested to contribute to the organization of thunderstorm clouds into large clusters of rain-producing areas. The widespread, heavy rainfall can then cause flooding. To better predict such flooding in numerical weather models, having a precise observational basis for cold pool properties is essential — yet currently missing in equatorial Africa. We here provide such an observational benchmark by analyzing thousands of cold pools using timeseries of near-surface temperature, wind, humidity and precipitation. We additionally show that the cold pools can even be detected from satellite data when analyzing abrupt changes in cloud top temperature. Such satellite-based detection could open for cold pool studies across all tropical land areas — of great practical relevance to the prediction of thunderstorm clusters.

1. Introduction

Convective cold pools (CPs) are caused by the evaporation of rainfall beneath deep convective clouds (Zuidema et al., 2017). The resultant denser air volume spreads out laterally along the surface and can cause a so-called “gust front” (GF) along its edges (Charba, 1974). The GF features strong horizontal and vertical winds along with moisture and temperature anomalies which together can give rise to additional deep convective events, for example, under collisions (Feng et al., 2015; Purdom, 1976). CPs are thus important agents in mediating interactions between deep convective cells and thus the self-organization of thunderstorm systems (Haerter et al., 2019; Jensen et al., 2021; Simpson, 1980; Tompkins, 2001b).

Recent idealized cloud-resolving and large-eddy simulations have provided new insight into CP structure and dynamics, such as on required mesh resolution (Fiévet et al., 2022), moisture rings (Drager et al., 2020; Langhans & Romps, 2015), or general interaction mechanisms (Haerter et al., 2020; Meyer & Haerter, 2020; Tompkins, 2001a; Torri et al., 2015), and triggered a range of simplified conceptual models (Böing, 2016; Haerter, 2019; Haerter et al., 2019; Niehues et al., 2022; Nissen & Haerter, 2021), which may help elucidate organizing mechanisms. New methods of CP detection in numerical studies have also been developed which help automatize the tracking of GFs and their interactions (Fournier & Haerter, 2019; Gentine et al., 2016; Henneberg et al., 2020; Hoeller, Fiévet, & Haerter, 2024; Hoeller, Fiévet, et al., 2024; Torri & Kuang, 2019).

© 2024. The Authors.

This is an open access article under the terms of the [Creative Commons Attribution License](https://creativecommons.org/licenses/by/4.0/), which permits use, distribution and reproduction in any medium, provided the original work is properly cited.

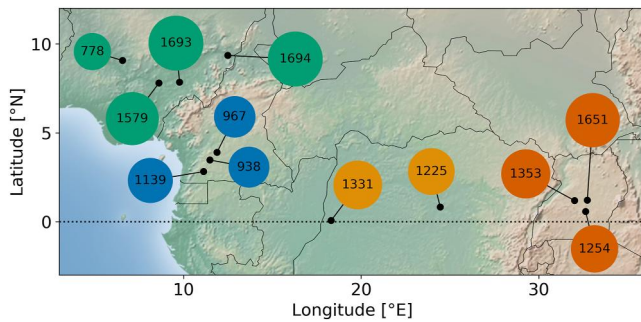


Figure 1. Weather station data employed. Map of equatorial Africa showing station locations (filled black circles). Numbers within colored circles and the size of the circle area represent available days of station data with a complete record of air temperature. Stations are grouped into four regions denoted by the colored circles: Cameroon (blue), Democratic Republic of Congo (yellow), Nigeria (green), Uganda (red).

Despite this progress in numerical and theoretical work, direct measurements of CPs are still limited to specific geographic regions, such as the tropical and sub-tropical ocean (Chandra et al., 2018; Vogel, 2017; Vogel et al., 2021; Zipser, 1977; Zuidema et al., 2012), mid-latitude continental regions in Central Europe (Kirsch et al., 2021; Kruse et al., 2022) or North America (Mueller & Carbone, 1987; Wakimoto, 1982; Engerer et al., 2008; Hitchcock et al., 2019; van den Heever et al., 2021), and — with a focus on dust storms — semi-arid tropical regions (Caton Harrison et al., 2021; Emmel et al., 2010; Redl et al., 2015).

Indeed, the importance of collecting information on CPs and precipitation in deep tropical regions has been pointed out (Adams et al., 2015) but systematic, climatological studies on CPs in such regions are still rare or lacking. This may partially be due to difficult environmental conditions which pose challenging demands on equipment and maintenance (Parker et al., 2008). Also the availability of funds may hinder systematic long-term campaigns in some regions. A notable exception is the trans-African hydro-meteorological observatory (TAHMO) which offers a promising network of station measurements in many sub-Saharan African countries (van de Giesen et al., 2014). Using a range of stations from the TAHMO network, we here present a climatology of CP measurements for equatorial Africa and compare findings to previous work in other geographic regions.

Using a range of stations from the TAHMO network, we here present a climatology of CP measurements for equatorial Africa and compare findings to previous work in other geographic regions.

2. Data

2.1. Station Data

We utilize data from twelve ATMO41 automatic weather stations (AWS) (Figure 1), operated by TAHMO. The stations are situated in Cameroon, the Democratic Republic of Congo (DR Congo), Nigeria, and Uganda. To investigate the influence of regional climatic differences on CPs, we group stations according to their respective deployment countries in our analysis.

The AWS provide data at a five-minute temporal resolution. All stations are installed at an approximate height of two m above the surface. We employ the station records of precipitation, atmospheric pressure, air temperature, relative humidity, and wind gust speed. ATMO41 determines the latter by measuring instantaneous wind speed every 10 seconds and outputting the maximum instantaneous wind speed value within any given five-minute interval. If an instantaneous wind speed is larger than eight times the running average of the previous 10 instantaneous measurements, the measurement is rejected. While this method may prevent spurious spikes in the wind record under normal conditions, it can cause missing wind data in cases of large and sudden wind changes. Given the frequent occurrence of such strong wind variations associated with CP GFs, approximately 22% of all identified CPs have an incomplete wind record.

We analyze the data recorded by these AWSs from 1 January 2019, to 30 September 2023. As not all AWSs were operational throughout the entire period, we limit our analysis for each station to days with complete air temperature records. Additionally, we require the air temperature to be recorded for a minimum of 10 consecutive minutes from the previous day and for the subsequent 120 min on the following day. The resulting number of analysis days per station is indicated in Figure 1. In total, we analyzed 15,602 days and thus nearly 43 years of station data.

Based on the station-measured variables, we additionally compute both mixing ratio, r and saturated mixing ratio, r_{sat} (see Text S1 in Supporting Information S1), and derive the specific humidity, $q \equiv r/(1 + r)$ and the specific humidity deficit, $q_D \equiv q_{sat} - q = r_{sat}/(1 + r_{sat}) - q$.

2.2. Satellite Data

Apart from the station data, we utilize infrared brightness temperature measurements which we derive from satellite-measured effective radiances. The radiances are extracted from Meteosat Second Generation (MSG) 0° products provided by the European Organization for the Exploitation of Meteorological Satellites (EUMETSAT). The data has a baseline repeat cycle of 15 min and a spatial resolution of 3 km in the sub-satellite point. To convert

the radiances to brightness temperatures we employ equation 5.3 and the corresponding regression coefficients of EUMETSAT (2012).

3. Methods

3.1. Cold Pool Detection Algorithm

(i) Temperature criterion

A potential CP event is detected at a given time t if three conditions apply: (a), similar to Kirsch et al. (2021) we require a substantial temperature decrease $\Delta T \leq -2$ K, within the 20 min window from $t - 5$ min to $t + 15$ min. Additionally, we require (b), the decrease of ΔT to be monotonic and (c), $T(t) - T(t - 5 \text{ min}) \leq -0.5$ K.

While the chosen conditions minimize the risk of high false alarm rates due to typical diurnal temperature changes, some weak or dissipating CP GFs might be missed. Choosing a ΔT of -1.5 K as used by Kruse et al. (2022) leads to approximately 28% more identifications, marginally weakening CP-associated median temperature and specific humidity decreases by 11%–12%, without impacting overall results.

(ii) Wind criterion

To confirm detected potential CP events, we adapt the wind criterion introduced by Kruse et al. (2022). For this purpose, we compute the wind gust speed anomaly for each time t as

$$\Delta u_g(t) \equiv u_g(t) - \bar{u}_g(t), \quad (1)$$

where u_g is the wind gust speed (see Section 2.1) and \bar{u}_g its centered 2-hr running mean, that is, the mean value of the 25 wind gust speeds recorded during the corresponding 2-hr window.

For a potential CP event at time t we identify the maximum wind gust speed anomaly, Δu_g^{\max} , between $t - 20$ min and $t + 40$ min. We retain it as potential CP event if

$$\Delta u_g^{\max} \geq \overline{\Delta u_g}(t) + n_w \sigma_{\Delta u_g}(t), \quad (2)$$

with $n_w = 3$, the centered 24-hr running mean of the wind gust speed anomaly, $\overline{\Delta u_g}$, and the corresponding 24-hr running standard deviation, $\sigma_{\Delta u_g}$. While higher n_w mainly increase the number of missed CPs, smaller n_w values give rise to more false positive detections. For instance, using $n_w = 2$ would yield 12% more identifications, with 2.5 times as many events that cannot be attributed to convective events in satellite data and, therefore, are rejected in step (iv).

As the potential CP onset is defined based on the temperature criterion, we also search for associated wind gusts in a 20 min time window before this onset. We choose 20 min rather than the 10 min used by Kruse et al. (2022) since our temperature criterion involves a minimum decrease of -0.5 K within 5 min to define the onset of potential CPs and might thus delay the onset in comparison to Kruse et al. (2022). The 40 min time window after potential CP onset allows significant wind offsets while ensuring a temporal relation between ΔT and Δu_g^{\max} . Halving both time windows would reduce CP identifications by about 7%, with negligible impact on overall results.

In case of missing wind gust speed anomalies between $t - 20$ min and $t + 40$ min, we identify the maximum wind gust speed, u_g^{\max} within this time window rather than Δu_g^{\max} and retain the event as potential CP if

$$u_g^{\max} \geq \bar{u}_g(t - 80 \text{ min}) + n_{\text{miss}} \sigma_{u_g}(t - 80 \text{ min}), \quad (3)$$

with $n_{\text{miss}} = 2$, the centered 2-hr running mean, \bar{u}_g , and the corresponding standard deviation, σ_{u_g} . Approximately 25% of the detected CPs is identified based on Equation 3 rather than Equation 2. By evaluating \bar{u}_g and σ_{u_g} 80 min before potential CP onset, we keep again a 20 min offset between the onset and the 2-hr time window of the reference values. Since portions of the wind record are missing, we choose n_{miss} conservatively. Yet, neither the number of identifications nor the results are sensitive to the selection of n_{miss} .

If no wind gust speed data has been recorded between $t - 20$ min and $t + 40$ min, or if the reference values $\bar{u}_g(t - 80 \text{ min})$ and $\bar{u}_g(t - 80 \text{ min})$ could not be computed due to missing data, we consider the event as "no CP."

Differing from Kruse et al. (2022), we evaluate the wind criterion based on wind gust speed rather than wind speed. Since we work with station data with a temporal resolution of 5 min in contrast to 1 min in (Kruse et al., 2022), we find wind gust speed a better indicator for CP GFs than wind speed.

(iii) Duplicate detection check

Often, a CP fulfills the defined criteria (i) and (ii) not only at time t , but also at subsequent time steps. Depending on the evolution of temperature and wind gust speed behind the CP GF, time steps in which the criteria are met can even be separated from each other by time steps in which the criteria are not met. To avoid duplicate detection of a given CP, we drop detected events if at least one other event was detected within 20 min before that particular event. Given the variety of environmental conditions under which we observe CPs at our station locations, we find this definition to be more permissive than the absolute 60 min time window after detected temperature decreases, within which Kirsch et al. (2021) considers any detected decrease as part of the same event.

(iv) Space-borne verification

In some cases, especially during the Nigerian dry season, neither condition (i) nor (ii) may suffice to completely prevent false positive detections caused by strong diurnal temperature changes. Consequently, we validate each detected event using satellite-measured 10.8 μm brightness temperatures, $BT_{10.8}$. We consider an event at time t as CP if the minimum $BT_{10.8}$ recorded between $t - 3$ hr and t within a 2° radius around the station is less than 240 K.

The parameters of the verification ensure the presence of temporally related convective events in the vicinity of the potential CP event. Applying this verification to all detected events, 71 false positive detections are identified and dropped. Reducing the radius around the station from 2° to 1.5° would increase the number of rejected events to 85.

3.2. Determination of Cold Pool Anomalies

We analyze the effects of a detected CP with respect to different station-measured meteorological variables by considering a time window relative to CP onset, t_0 , from $t_0 - 40$ min to $t_0 + 120$ min. Within this time window, we evaluate the CP associated anomalies $y'(t) \equiv y(t) - y_{ref}$ for a meteorological variable y based on an unperturbed reference state y_{ref} , which we define as the temporal mean of instantaneous measurements in a time interval before CP onset. Since the onset is defined based on the temperature drop and thus could be different for other variables, we choose the time interval from $t_0 - 40$ min to $t_0 - 20$ min to keep a sufficient margin of 20 min to the CP onset while preserving the required temporal proximity. To minimize any distortion of the reference state through the diurnal cycle, we deviate from this definition only for temperature anomalies and follow the approach of the refined temperature drop from Kruse et al. (2022) instead, that is, we consider the maximum temperature of the two measurements in the 10 min time window preceding the CP onset as unperturbed reference temperature.

Due to the coarser temporal resolution, we extend the time window in which we analyze the anomalies before CP onset to 60 min for satellite-measured 10.8 μm brightness temperatures, $BT_{10.8}$, and define the reference brightness temperature, $BT_{10.8}^{ref}$, as the mean of the three observations in the time interval from $t_0 - 60$ min to $t_0 - 30$ min. As there might not be a brightness temperature observation at the station-derived CP onset, t_0 , we define the closest satellite time step as \hat{t}_0 and measure the CP time relative to it. The brightness temperature anomalies, $BT'_{10.8}$, are then computed analogously to those for station-measured variables. Moreover, to further investigate the space-borne CP signature, we additionally determine the temporal change of $BT'_{10.8}$, as $\Delta BT'_{10.8}(t) = BT'_{10.8}(t) - BT'_{10.8}(t - 15 \text{ min})$.

The overall impact of the described parameter choices on the observed anomalies is relatively weak. For instance, doubling the time interval for computing the unperturbed reference state from 20 to 40 min, while maintaining the 20 min offset to CP onset, would result in a 1.4% enhancement in the median specific humidity drop. Similarly, calculating the unperturbed reference temperature based on the mean value of the four measurements before CP onset, instead of using the maximum of the previous two, would lead to a 1.3% reduction in the median temperature drop.

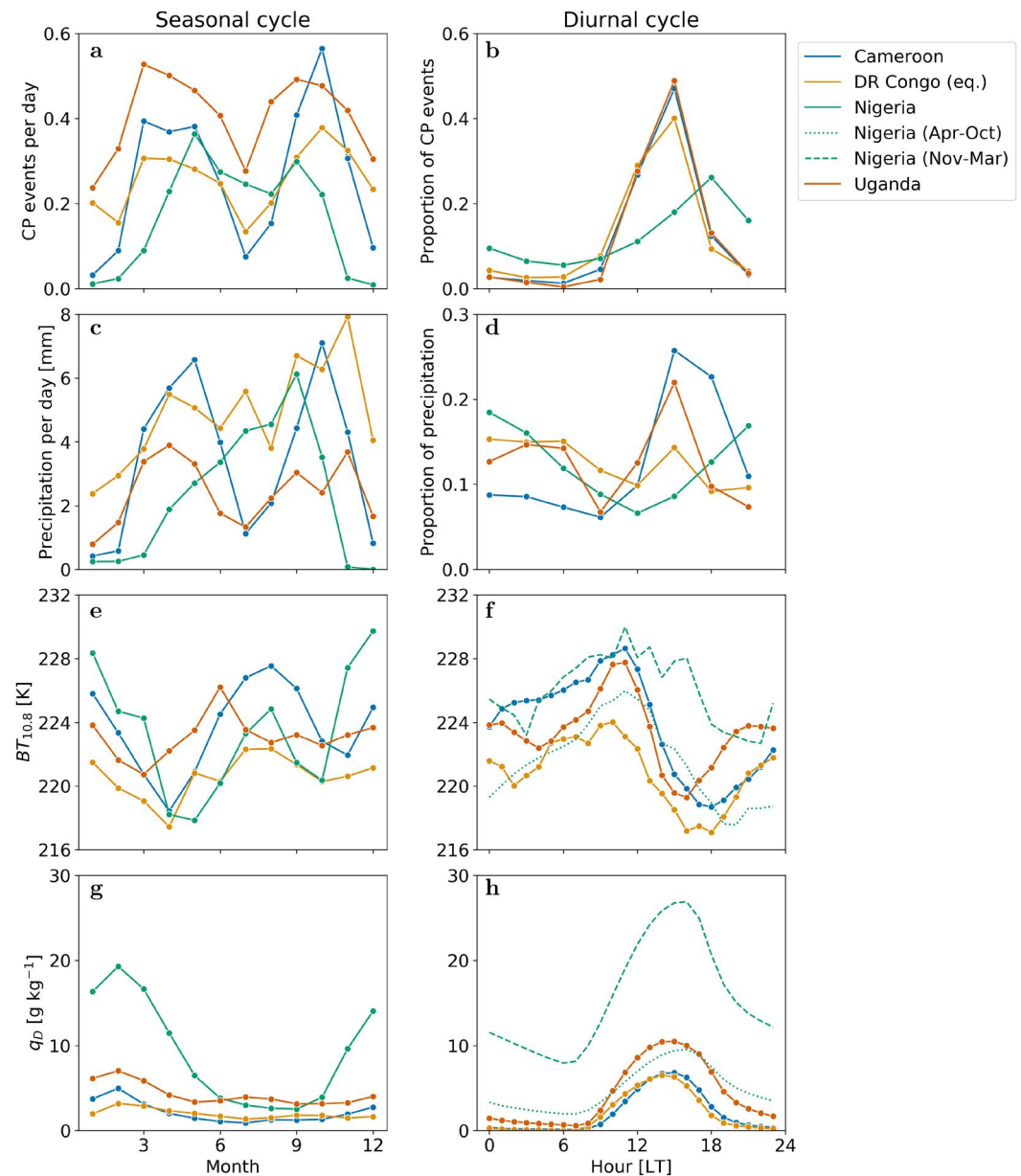


Figure 2. Observed seasonal and diurnal cycles. Line colors indicate distinct sub-regions (see legend). a, Mean number of daily cold pool (CP) events for each month. Lines interpolate linearly between markers to facilitate the interpretation; colors indicate different regions. The number of CP events is normalized based on the number of analyzed days per month and region. b, Proportion of CP events at different times of the day. Each marker represents the proportion of CP events observed within a given 3-hr time interval, starting with the interval [0,3) for the marker at 0 LT. c, Analogous to (a) but for precipitation. d, Analogous to (b) but for precipitation. e, Mean $10.8 \mu\text{m}$ brightness temperature, $BT_{10.8}$, of deep clouds ($BT_{10.8} \leq 240$ K) for each month. f, Mean $BT_{10.8}$ of deep clouds at different times of the day. The two lines for Nigeria represent rainy (Apr–Oct, dotted) and dry months (Nov–Mar, dashed). g, Analogous to (e) but for mean specific humidity deficit, q_D . h, Analogous to (f) but for mean q_D .

4. Results

4.1. Seasonal and Diurnal Cycle of Observed Cold Pools

First, we derive the seasonal and diurnal cycles of CPs in the different sub-regions (Figure 1) and relate them with precipitation, convection depth and moisture conditions (Figure 2). With about 0.3–0.6 CPs per day in the high seasons (Figure 2a, Table S2 in Supporting Information S1), equatorial Africa boasts particular CP

abundance compared to previous climatologies in other continental regions with about 0.1–0.3 CPs per day (Kirsch et al., 2021; Kruse et al., 2022; Redl et al., 2015). In every sub-region, the number of CPs peaks twice during the course of the year with a first maximum between March and May and a second maximum between September and October. The bi-modality in the annual cycle of CPs largely corresponds to the latitudinal migration of the Inter-Tropical Convergence Zone (ITCZ) as reflected in the precipitation seasonal cycles (Figure 2c). However, we note that precipitation may not explain all the features of the annual cycle of CPs and the differences between sub-regions. For instance, Nigeria presents a single precipitation peak in September whereas CP occurrence peaks in both May and September. There, the strong CP activity during May may be related to the combination of deeper convection (Figure 2e) fed by high equivalent potential temperatures (θ_E ; Figure S1 in Supporting Information S1) and of higher low-level specific humidity deficit (q_D ; Figure 2g) boosting rain evaporation. We also note that Uganda receives the least precipitation among sub-regions while experiencing most frequent CPs during the year. We attribute the larger number of CPs in Uganda to generally drier conditions at low levels (Figure 2g).

The diurnal cycle of CPs strongly peaks between 15 LT and 18 LT in all regions except Nigeria, where the peak is reached between 18 LT and 21 LT (Figure 2b). The high CP activity during the afternoon can be directly related to the afternoon peak in (deep) convection, highlighted by maxima in precipitation (Figure 2d) and lower brightness temperatures (Figure 2f). Consistently with earlier studies (Andrews et al., 2023; Camberlin et al., 2018; Zhang et al., 2016), precipitation shows secondary nocturnal peaks in Uganda and Congo, and remains high during the night in Nigeria, whereas the proportion of CPs displays local minima during these hours. This mismatch between precipitation and CPs is likely to be related to both the decline of convection during the night (leading to weaker rainfall intensities and downdrafts) and to moister conditions at the surface (reducing rainfall evaporative cooling; Figure 2h) which both inhibit CP formation (Zuidema et al., 2017).

4.2. Observed Cold Pool Characteristics

We further characterize equatorial African CPs by relating their temperature and moisture anomalies (defined in Section 3.2). On average, such CPs are accompanied by 5 K drops in temperature — compared to 3 K in Germany; Kirsch et al. (2021) — occurring within approximately 30 min, with little variability among sub-regions (Figure 3a, Table S2 in Supporting Information S1). In distinction to Kirsch et al. (2021), the CPs we analyze here generally show decreases in specific humidity after CP passage (Figure 3d). Interestingly, we find that the magnitude of this decrease is smaller for the elevated (Table S1 in Supporting Information S1) stations of Uganda (-1 g kg^{-1}) characterized by less deep convection (Figures 2e and 2f) and drier low-level environments (Figures 2g and 2h) compared to the other sub-regions (about -3 g kg^{-1}). Less deep convection is likely to be associated with lower (relative to the ground) convective downdrafts origins (Zuidema et al., 2017), importing less upper-level dry air to the surface. This may combine with enhanced rain evaporation due to drier environments, thus explaining the more modest reduction in specific humidity over Uganda. When considering the 25% driest (moistest) low-level pre-CP environments, we further evidence the large impact of moisture conditions, and thus of rain evaporation, on CP temperature and moisture anomalies in all sub-regions (Figures 2b, 2c, 2e and 2f): CP anomalies typically are 3 K cooler and 2 g kg^{-1} moister in the driest pre-CP conditions than in the moistest pre-CP conditions. We note weak maxima in specific humidity occurring few minutes after CP onset — so-called moisture rings (Langhans & Romps, 2015; Schlemmer & Hohenegger, 2016; Tompkins, 2001a) — over Cameroon, Uganda and Congo for the driest pre-CP environments. Finally, the temporal evolution of q_D (Figures 3g–3i) reveals that, in the driest environments, rain evaporation may not be sufficient to saturate the low-level air — similar to Germany; Kirsch et al. (2021).

Addressing CP cloud characteristics, we find that 96% (Uganda) to 100% (Congo) of CP GFs are accompanied by shallow or deep convective clouds (Figure S2a in Supporting Information S1). More specifically, CPs are generally accompanied by a strong decrease in $BT_{10.8}$ (Figure 4a), for example, reaching 36 K in Congo. The $BT_{10.8}$ minimum is typically achieved 30–45 min after CP onset. While this minimum is delayed w.r.t. the CP onset, we find a minimum of the time derivative of $BT'_{10.8}$ to be synchronized with CP onset in all sub-regions (Figure 4b). This observation suggests that CPs in equatorial Africa, and potentially other regions, might be detectable from space-borne satellite data.

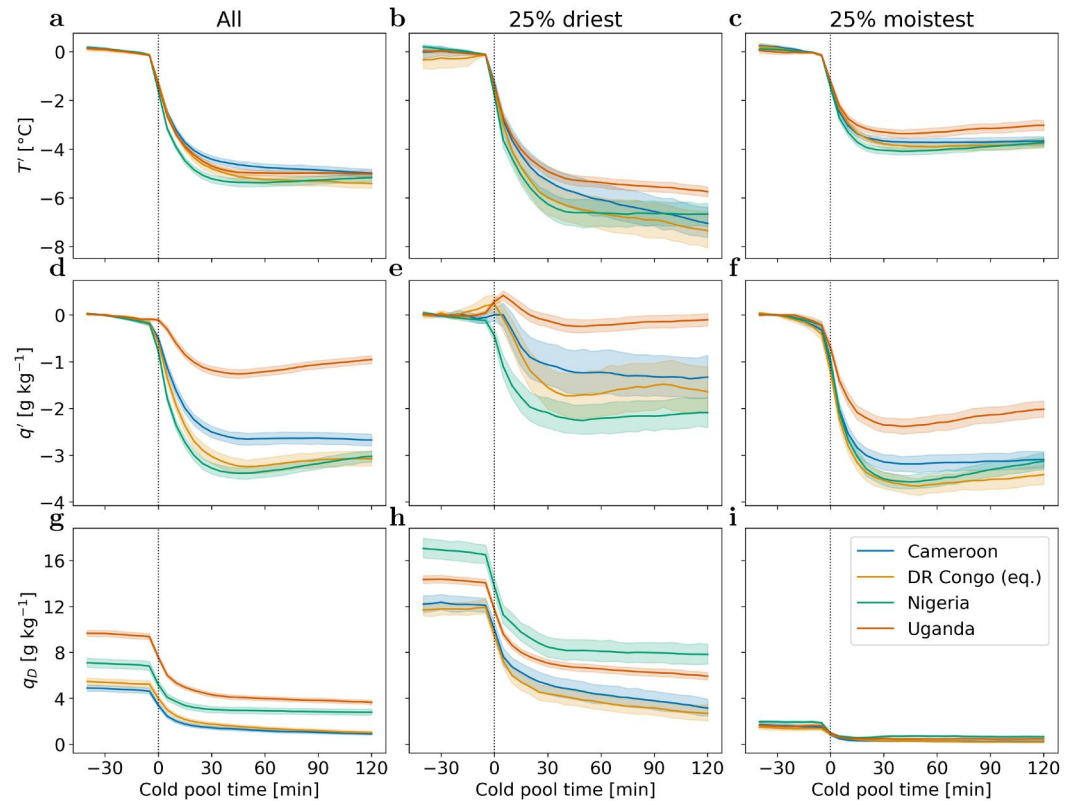


Figure 3. Station-derived cold pool (CP) properties relative to CP onset, t_0 . a, Mean temperature anomalies, T' , for different regions; shading indicates the 95% confidence interval. b, Analogous to (a) but for the 25% driest pre-CP environments of each region w.r.t. the reference specific humidity deficit, q_D^{ref} , prior to t_0 . c, Analogous to (b) but for the 25% moistest pre-CP environments. d–f, Analogous to (a)–(c) but for mean specific humidity anomalies, q' . g–i, Analogous to (a)–(c) but for mean specific humidity deficits, q_D . Note that only timeseries of CPs, where t_0 is more than 120 min apart from other CP onsets, are included in the analysis.

5. Summary and Discussion

The present study provides multi-year statistics of cold pool characteristics in equatorial Africa, based on five-minute near-surface weather data. Using detection methods similar to those in previous studies focused on mid-latitude continental regions, key findings include that temperature drops upon gust front passage often exceed 5 K and specific humidities typically decrease by more than 3 g kg^{-1} . Weak moisture rings can only be identified in some of the sub-regions for the driest pre-cold pool environments — in agreement with Kruse et al. (2022) for data in the Netherlands where moisture rings were generally not detected.

Seasonally, the rate of cold pool occurrence roughly follows precipitation statistics. Diurnally, in contrast, cold pool occurrence sharply peaks during the drier late afternoon times, departing from the weak precipitation diurnal cycle. We suggest this may be due to the nocturnal boundary layer often being close to saturation, thus diminishing cold pool occurrence there. This finding may have important implications for thunderstorm organization through cold pool activity: the limited time window where cold pools actually occur during the day means that self-organization may be limited to relatively short periods of the day. One could speculate that it is the lack of cold pool activity that limits the duration of mesoscale convective systems, often less than 12 hr, rather than the precipitation itself — which is more spread out over the day. Yet, further investigations are needed to substantiate this claim, for example, by using additional radiosonde data to explore the vertical coordinate. Future studies should also analyze if deep convection is more scattered during nocturnal periods when fewer cold pools occur. Comparisons with oceanic cold pools and their organizational effects, which tend to be weaker (Zuidema et al., 2017), would be insightful.

Our cold pool detection algorithm can be adapted to other regions, provided that there are in-situ weather stations measuring surface wind and temperature with at least 5-min temporal resolution. However, in-situ weather

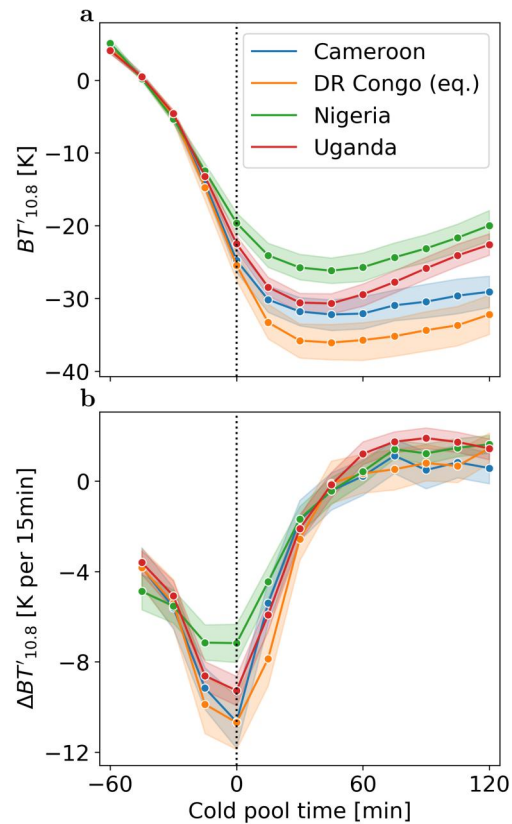


Figure 4. Space-borne signatures of cold pools (CPs) relative to CP onset, t_0 . a, Mean $10.8 \mu\text{m}$ brightness temperature anomalies, $BT'_{10.8}$, of station-derived CPs for different regions; shading indicates the 95% confidence interval. b, Analogous to (a) but for the corresponding derivative $\Delta BT'_{10.8}$.

stations meeting this requirement are still limited in the tropics, whereas cold pools are abundant. Encouragingly, our findings may have implications for satellite-based cold pool detection: we show that gust front passage clearly correlates with discontinuities in satellite-derived brightness temperature. We generally observe a significant decrease in brightness temperatures around the time of the gust front passage, with maximum decrease rates at the station-derived cold pool onset. Our findings thus suggest that cold pools in equatorial Africa, and potentially other regions, could be directly detectable from geostationary satellite data on a continental scale. While significant decreases in brightness temperature alone are not a sufficient criterion for identifying cold pool gust fronts, the concurrence with spatiotemporal patterns like radially spreading cloud arcs and rapidly expanding deep convection (Text S2, Figure S3 in Supporting Information S1) could aid neural networks, such as those developed by Hoeller, Fiévet, et al. (2024), in limiting the number of false positive detections. Even in cases where not all parts of a cold pool gust front exhibit brightness temperature drops (Figure S2b in Supporting Information S1), the presence of such spatiotemporal patterns may enable the neural networks to accurately track the gust front.

Conflict of Interest

The authors declare no conflicts of interest relevant to this study.

Data Availability Statement

Both the code for the cold pool gust front identification and the processed data sets are licensed under Creative Commons Attribution 4.0 International and were used in version 2.0 (Hoeller, Haerter, & Da Silva, 2024). The raw data of the automatic weather stations was provided by TAHMO and is not publicly available. For more

information about the data, please visit <https://tahmo.org/climate-data/>. Interested parties may contact info@tahmo.org for this data. The satellite-observed radiances were extracted from Meteosat Second Generation (MSG) 0° products (<https://navigator.eumetsat.int/product/EO:EUM:DAT:MSG:HRSEVIRI>), provided by EUMETSAT without a license on an unrestricted basis. Figures were made with Matplotlib version 3.5.2 (Caswell et al., 2022; Hunter, 2007) and seaborn version 0.12.2 (Waskom, 2021).

Acknowledgments

The authors gratefully acknowledge funding by a grant from the VILLUM Foundation (grant number: 13168) and the European Research Council (ERC) under the European Union's Horizon 2020 research and innovation program (grant number: 771859) and the Novo Nordisk Foundation Interdisciplinary Synergy Program (Grant NNF19OC0057374). This work used resources of the Deutsches Klimarechenzentrum (DKRZ), granted by its Scientific Steering Committee (WLA) under project ID bb1166. Additionally, the authors thank the Trans-African Hydro-Meteorological Observatory (TAHMO) for the provision of meteorological data. Interested parties may contact info@tahmo.org for these data. Open Access funding enabled and organized by Projekt DEAL.

References

- Adams, D. K., Fernandes, R. M., Holub, K. L., Gutman, S. I., Barbosa, H. M., Machado, L. A., et al. (2015). The amazon dense gns meteorological network: A new approach for examining water vapor and deep convection interactions in the tropics. *Bulletin of the American Meteorological Society*, 96(12), 2151–2165. <https://doi.org/10.1175/bams-d-13-00171.1>
- Andrews, P. C., Cook, K. H., & Vizy, E. K. (2023). Mesoscale convective systems in the Congo Basin: Seasonality, regional, and diurnal cycles. *Climate Dynamics*, 62, 1–22. <https://doi.org/10.1007/s00382-023-06903-7>
- Böing, S. J. (2016). An object-based model for convective cold pool dynamics. *Mathematics of Climate and Weather Forecasting*, 2(1). <https://doi.org/10.1515/mcwf-2016-0003>
- Camberlin, P., Gitau, W., Planchon, O., Dubreuil, V., Funatsu, B. M., & Philippon, N. (2018). Major role of water bodies on diurnal precipitation regimes in Eastern Africa. *International Journal of Climatology*, 38(2), 613–629. <https://doi.org/10.1002/joc.5197>
- Caswell, T. A., Droettboom, M., Lee, A., de Andrade, E. S., Hoffmann, T., Klymak, J., et al. (2022). matplotlib/matplotlib: Release (version 3.5.2) [software]. *Zenodo*. <https://doi.org/10.5281/zenodo.6513224>
- Caton Harrison, T., Washington, R., & Engelstaedter, S. (2021). Satellite-derived characteristics of Saharan cold pool outflows during boreal summer. *Journal of Geophysical Research: Atmospheres*, 126(3), e2020JD033387. <https://doi.org/10.1029/2020jd033387>
- Chandra, A. S., Zuidema, P., Krueger, S., Kochanski, A., de Szoeke, S. P., & Zhang, J. (2018). Moisture distributions in tropical cold pools from equatorial indian ocean observations and cloud-resolving simulations. *Journal of Geophysical Research: Atmospheres*, 123(20), 11–445. <https://doi.org/10.1029/2018jd028634>
- Charba, J. (1974). Application of gravity current model to analysis of squall-line gust front. *Monthly Weather Review*, 102(2), 140–156. [https://doi.org/10.1175/1520-0493\(1974\)102<0140:aogcmt>2.0.co;2](https://doi.org/10.1175/1520-0493(1974)102<0140:aogcmt>2.0.co;2)
- Drager, A. J., Grant, L. D., & van den Heever, S. C. (2020). Cold pool responses to changes in soil moisture. *Journal of Advances in Modeling Earth Systems*, 12(8), e2019MS001922. <https://doi.org/10.1029/2019ms001922>
- Emmel, C., Knippertz, P., & Schulz, O. (2010). Climatology of convective density currents in the southern foothills of the atlas mountains. *Journal of Geophysical Research: Atmospheres*, 115(D11). <https://doi.org/10.1029/2009jd012863>
- Engerer, N. A., Stensrud, D. J., & Coniglio, M. C. (2008). Surface characteristics of observed cold pools. *Monthly Weather Review*, 136(12), 4839–4849. <https://doi.org/10.1175/2008mwr2528.1>
- EUMETSAT. (2012). The conversion from effective radiances to equivalent brightness temperatures (version 1). Retrieved from https://www-cdn.eumetsat.int/files/2020-04/pdf_effect_rad_to_brightness.pdf
- Feng, Z., Hagos, S., Rowe, A. K., Burleyson, C. D., Martini, M. N., & de Szoeke, S. P. (2015). Mechanisms of convective cloud organization by cold pools over tropical warm ocean during the AMIE/DYNAMO field campaign. *Journal of Advances in Modeling Earth Systems*, 7(2), 357–381. <https://doi.org/10.1002/2014ms000384>
- Fiévet, R., Meyer, B., & Haerter, J. O. (2022). On the sensitivity of convective cold pools to mesh resolution. *Earth and Space Science Open Archive*, 24. <https://doi.org/10.1002/essoar.10512297.1>
- Fournier, M. B., & Haerter, J. O. (2019). Tracking the gust fronts of convective cold pools. *Journal of Geophysical Research: Atmospheres*, 124(21), 11103–11117. <https://doi.org/10.1029/2019jd030980>
- Gentine, P., Garelli, A., Park, S., Nie, J., Torri, G., & Kuang, Z. (2016). Role of surface heat fluxes underneath cold pools. *Geophysical Research Letters*, 43(2), 874–883. <https://doi.org/10.1002/2015gl067262>
- Haerter, J. O. (2019). Convective self-aggregation as a cold pool-driven critical phenomenon. *Geophysical Research Letters*, 46(7), 4017–4028. <https://doi.org/10.1029/2018gl081817>
- Haerter, J. O., Böing, S. J., Henneberg, O., & Nissen, S. B. (2019). Circling in on convective organization. *Geophysical Research Letters*, 46(12), 7024–7034. <https://doi.org/10.1029/2019gl082092>
- Haerter, J. O., Meyer, B., & Nissen, S. B. (2020). Diurnal self-aggregation. *npj Climate and Atmospheric Science*, 3(1), 30. <https://doi.org/10.1038/s41612-020-00132-z>
- Henneberg, O., Meyer, B., & Haerter, J. O. (2020). Particle-based tracking of cold pool gust fronts. *Journal of Advances in Modeling Earth Systems*, 12(5). <https://doi.org/10.1029/2019ms001910>
- Hitchcock, S. M., Schumacher, R. S., Herman, G. R., Coniglio, M. C., Parker, M. D., & Ziegler, C. L. (2019). Evolution of pre-and postconvective environmental profiles from mesoscale convective systems during pecan. *Monthly Weather Review*, 147(7), 2329–2354. <https://doi.org/10.1175/mwr-d-18-0231.1>
- Hoeller, J., Fiévet, R., Engelbrecht, E., & Haerter, J. O. (2024). U-net segmentation for the detection of convective cold pools from cloud and rainfall fields. *Journal of Geophysical Research: Atmospheres*, 129(1), e2023JD040126. <https://doi.org/10.1029/2023jd040126>
- Hoeller, J., Fiévet, R., & Haerter, J. O. (2024). Detecting cold pool family trees in convection resolving simulations. *Journal of Advances in Modeling Earth Systems*, 16(1), e2023MS003682. <https://doi.org/10.1029/2023ms003682>
- Hoeller, J., Haerter, J. O., & Da Silva, N. (2024). Identification algorithm for cold pool gust fronts in weather station data from equatorial Africa (version 2.0) [software]. *Zenodo* <https://doi.org/10.5281/zenodo.10117788>
- Hunter, J. D. (2007). Matplotlib: A 2D graphics environment. *Computing in Science and Engineering*, 9(3), 90–95. <https://doi.org/10.1109/MCSE.2007.55>
- Jensen, G. G., Fiévet, R., & Haerter, J. O. (2021). The diurnal path to persistent convective self-aggregation. arXiv preprint arXiv:2104.01132.
- Kirsch, B., Ament, F., & Hohenegger, C. (2021). Convective cold pools in long-term boundary layer mast observations. *Monthly Weather Review*, 149(3), 811–820. <https://doi.org/10.1175/mwr-d-20-0197.1>
- Kruse, I. L., Haerter, J. O., & Meyer, B. (2022). Cold pools over The Netherlands: A statistical study from tower and radar observations. *Quarterly Journal of the Royal Meteorological Society*, 148(743), 711–726. <https://doi.org/10.1002/qj.4223>
- Langhans, W., & Romps, D. M. (2015). The origin of water vapor rings in tropical oceanic cold pools. *Geophysical Research Letters*, 42(18), 7825–7834. <https://doi.org/10.1002/2015gl065623>

- Meyer, B., & Haerter, J. O. (2020). Mechanical forcing of convection by cold pools: Collisions and energy scaling. *Journal of Advances in Modeling Earth Systems*, 12(11). n/a–n/a. <https://doi.org/10.1029/2020MS002281>
- Mueller, C. K., & Carbone, R. E. (1987). Dynamics of a thunderstorm outflow. *Journal of the Atmospheric Sciences*, 44(15), 1879–1898. [https://doi.org/10.1175/1520-0469\(1987\)044<1879:doato>2.0.co;2](https://doi.org/10.1175/1520-0469(1987)044<1879:doato>2.0.co;2)
- Niehues, J., Jensen, G. G., & Haerter, J. O. (2022). Self-organized quantization and oscillations on continuous fixed-energy sandpiles. *Physical Review E*, 105(3), 034314. <https://doi.org/10.1103/physreve.105.034314>
- Nissen, S. B., & Haerter, J. O. (2021). Circling in on convective self-aggregation. *Journal of Geophysical Research: Atmospheres*, 126(20), e2021JD035331. <https://doi.org/10.1029/2021jd035331>
- Parker, D. J., Fink, A., Janicot, S., Ngamini, J.-B., Douglas, M., Afiesimama, E., et al. (2008). The amma radiosonde program and its implications for the future of atmospheric monitoring over Africa. *Bulletin of the American Meteorological Society*, 89(7), 1015–1028. <https://doi.org/10.1175/2008bams2436.1>
- Purdum, J. F. (1976). Some uses of high-resolution goes imagery in the mesoscale forecasting of convection and its behavior. *Monthly Weather Review*, 104(12), 1474–1483. [https://doi.org/10.1175/1520-0493\(1976\)104<1474:suohrg>2.0.co;2](https://doi.org/10.1175/1520-0493(1976)104<1474:suohrg>2.0.co;2)
- Redl, R., Fink, A. H., & Knippertz, P. (2015). An objective detection method for convective cold pool events and its application to Northern Africa. *Monthly Weather Review*, 143(12), 5055–5072. <https://doi.org/10.1175/mwr-d-15-0223.1>
- Schlemmer, L., & Hohenegger, C. (2016). Modifications of the atmospheric moisture field as a result of cold-pool dynamics. *Quarterly Journal of the Royal Meteorological Society*, 142(694), 30–42. <https://doi.org/10.1002/qj.2625>
- Simpson, J. (1980). Downdrafts as linkages in dynamic cumulus seeding effects. *Journal of Applied Meteorology*, 19(4), 477–487. [https://doi.org/10.1175/1520-0450\(1980\)019<0477:dalide>2.0.co;2](https://doi.org/10.1175/1520-0450(1980)019<0477:dalide>2.0.co;2)
- Tompkins, A. M. (2001a). Organization of tropical convection in low vertical wind shears: The role of cold pools. *Journal of the Atmospheric Sciences*, 58(13), 1650–1672. [https://doi.org/10.1175/1520-0469\(2001\)058\(1650:ootcil\)2.0.co;2](https://doi.org/10.1175/1520-0469(2001)058(1650:ootcil)2.0.co;2)
- Tompkins, A. M. (2001b). Organization of tropical convection in low vertical wind shears: The role of water vapor. *Journal of the Atmospheric Sciences*, 58(6), 529–545. [https://doi.org/10.1175/1520-0469\(2001\)058<0529:ootcil>2.0.co;2](https://doi.org/10.1175/1520-0469(2001)058<0529:ootcil>2.0.co;2)
- Torri, G., & Kuang, Z. (2019). On cold pool collisions in tropical boundary layers. *Geophysical Research Letters*, 46(1), 399–407. <https://doi.org/10.1029/2018gl080501>
- Torri, G., Kuang, Z., & Tian, Y. (2015). Mechanisms for convection triggering by cold pools. *Geophysical Research Letters*, 42(6), 1943–1950. <https://doi.org/10.1002/2015gl063227>
- van de Giesen, N., Hut, R., & Selker, J. (2014). The Trans-African Hydro-Meteorological Observatory (TAHMO). *Wiley Interdisciplinary Reviews: Water*, 1(4), 341–348. <https://doi.org/10.1002/wat2.1034>
- van den Heever, S. C., Grant, L. D., Freeman, S. W., Marinescu, P. J., Barnum, J., Bukowski, J., et al. (2021). The Colorado State University Convective CLOUD Outflows and Updrafts Experiment (C³ LOUD-Ex). *Bulletin of the American Meteorological Society*, 102(7), E1283–E1305. <https://doi.org/10.1175/bams-d-19-0013.1>
- Vogel, R. (2017). *The influence of precipitation and convective organization on the structure of the trades* (Unpublished doctoral dissertation). Universität Hamburg Hamburg. Retrieved from https://pure.mpg.de/rest/items/item_2503092/component/file_2503091/content
- Vogel, R., Konow, H., Schulz, H., & Zuidema, P. (2021). A climatology of trade-wind cumulus cold pools and their link to mesoscale cloud organization. *Atmospheric Chemistry and Physics*, 21(21), 16609–16630. <https://doi.org/10.5194/acp-21-16609-2021>
- Wakimoto, R. M. (1982). The life cycle of thunderstorm gust fronts as viewed with Doppler radar and rawinsonde data. *Monthly Weather Review*, 110(8), 1060–1082. [https://doi.org/10.1175/1520-0493\(1982\)110<1060:tlcotg>2.0.co;2](https://doi.org/10.1175/1520-0493(1982)110<1060:tlcotg>2.0.co;2)
- Waskom, M. L. (2021). seaborn: Statistical data visualization. *Journal of Open Source Software*, 6(60), 3021. <https://doi.org/10.21105/joss.03021>
- Zhang, G., Cook, K. H., & Vizy, E. K. (2016). The diurnal cycle of warm season rainfall over West Africa. Part I: Observational analysis. *Journal of Climate*, 29(23), 8423–8437. <https://doi.org/10.1175/JCLI-D-15-0874.1>
- Zipser, E. (1977). Mesoscale and convective-scale downdrafts as distinct components of squall-line structure. *Monthly Weather Review*, 105(12), 1568–1589. [https://doi.org/10.1175/1520-0493\(1977\)105<1568:macdad>2.0.co;2](https://doi.org/10.1175/1520-0493(1977)105<1568:macdad>2.0.co;2)
- Zuidema, P., Li, Z., Hill, R. J., Bariteau, L., Rilling, B., Fairall, C., et al. (2012). On trade wind cumulus cold pools. *Journal of the Atmospheric Sciences*, 69(1), 258–280. <https://doi.org/10.1175/jas-d-11-0143.1>
- Zuidema, P., Torri, G., Muller, C., & Chandra, A. (2017). A survey of precipitation-induced atmospheric cold pools over oceans and their interactions with the larger-scale environment. *Surveys in Geophysics*, 38(6), 1–23. <https://doi.org/10.1007/s10712-017-9447-x>

References From the Supporting Information

- Bolton, D. (1980). The computation of equivalent potential temperature. *Monthly weather review*, 108(7), 1046–1053. [https://doi.org/10.1175/1520-0493\(1980\)108<1046:tcoept>2.0.co;2](https://doi.org/10.1175/1520-0493(1980)108<1046:tcoept>2.0.co;2)
- Wallace, J. M., & Hobbs, P. V. (2006). *Atmospheric science: an introductory survey* (Vol. 92). Elsevier.